Analysis of the Influence of Nozzle Structure and Hydraulic Parameters on the Cutting Efficiency of High-pressure Abrasive Water Jet (AWJ)

X. Zhu[1,2†], Z. Luo[1,2], Y. Luo[3], C. Shi[1,2] and L. Wang[3]

[1] School of Mechatronic Engineering, Southwest Petroleum University, Chengdu, 610500, PR China
[2] Oil and Gas Equipment Technology Sharing and Service Platform of Sichuan Province, Chengdu, 610500, PR China
[3] Well Control Emergency Rescue Response Center of CNPC Chuanqing Drilling Engineering Co., Ltd., Guanghan, Sichuan 618300, China

[†]Corresponding Author Email: zhuxh@swpu.edu.cn

ABSTRACT

The purpose of this study is to enhance the cutting efficiency of high-pressure abrasive water jet (AWJ) by optimizing nozzle structure and jet hydraulic parameters. To achieve nozzle structure optimization, CFD models of various nozzle shapes were established. The results indicate that the conduit length of conical nozzles has minimal impact on the cutting ability of the jet, while the conical nozzle with a taper angle of 40° exhibits excellent guiding characteristics. Furthermore, an infinite SPH AWJ cutting model with different hydraulic parameter settings was developed for the coupled numerical analysis of pump pressure, flow rate, and nozzle diameter. Through extensive numerical simulations, the study plotted curves of cutting depth and volume against pump pressure, flow rate, abrasive concentration, and nozzle diameter. The results show that, under specific hydraulic parameters, there exists an optimal abrasive concentration; and increasing the displacement leads to an increase in this optimal concentration. Furthermore, under constant pump pressure, increasing the nozzle diameter leads to an increase in flow rate. Additionally, both cutting depth and volume initially increase and then decrease, reaching their maximum values when the nozzle diameter ranges from 4mm to 5mm. The research findings provide a solid theoretical basis for abrasive jet cutting technology.

1. INTRODUCTION

Since the emergence of AWJ technology, the cutting efficiency of various materials has always been the focus of research both at home and abroad. The technology has been widely used due to its efficient cutting capability and low thermal impact (Pozzetti & Peters, 2018). Existing research primarily focuses on a number of key jet parameters, including pressure, jet velocity, standoff distance, abrasive particle type, etc (Thakur & Raut, 2023). The research methods mainly include theoretical research, experiments, and numerical simulations. However, there is a great difference in the understanding of the AWJ technology among scholars across the globe, leading to the proposal of different cutting theoretical models.

Bitted studied the erosion phenomenon and obtained the plastic fragmentation volume of a single particle when vertically impacting the target material based on the assumption of elastic-plasticity (Bitter, 1963). By studying the AWJ cutting of ceramics, glass, metal alloys and carbon fiber composites, Hashish (1984) has shown that there is no thermal deformation or delamination in the cut area of the material. Research results indicate that material properties have a significant impact on the efficiency and quality of AWJ cutting (Hashish, 1995), and that AWJ pressure has an impact on the cutting process (Hashish, 1989). Akkurt et al. (2004) explored the influence of AWJ on the deformation of workpieces with the same composition but different thicknesses (5 mm and 20 mm) at different feed rates and performed cutting on various materials such as pure aluminum, Al-6061 aluminum alloy, brass-353, AISI 1030, AISI 304 steel, etc.

Jegaraj and Babu (2005) studied and analyzed the influence of variations in the focusing nozzle diameter on the AWJ cutting process of 6063-T6 aluminum alloy. In the same year, Eltobgy simulated the cutting process of ductile materials with water jet through finite element mesh and SPH particle coupling simulation, and obtained

the relationship between the initial jet velocity and the maximum cutting depth of the ductile material (ElTobgy et al., 2005). In addition, the simulation and experimental results were compared to validate the feasibility of numerical simulation methods in cutting simulation. Babu et al. (2006) investigated the effects of single-grit size, pressure (150 MPa, 225 MPa, and 300 MPa), traverse speed, and abrasive flow rate (0.5 g/s, 1.0 g/s, and 1.5 g/s) on abrasive cutting. In the same year, Ahmet et al. (2006) studied the cutting of workpieces at different abrasive velocities (60, 80, 120, 150, 200, and 250 mm/min), and examined the profile, kerf geometry, and microstructure of the machined surface using surface profilometer and scanning electron microscope (SEM). Akkurt (2010) studied the cutting of brass-353 samples with different thicknesses (5 mm, 10 mm, 15 mm, and 20 mm) at different feed rates, determined the relationship between cutting depth (material thickness), feed rate, and deflection of the cutting edge geometry, and discussed the influence of material thickness on the surface roughness of the AWJ cutting section. Boud et al. (2014) studied the effects of abrasive velocity (3,000 mm/min, 4,000 mm/min, and 5,000 mm/min), standoff distance (10 mm and 25 mm), and jet pressure (40 KPSI and 50 KPSI) on surface structure and residual stress. Yuvaraj and Kumar (2016) explored the surface integrity of AWJ and cryogenic-assisted AWJ cutting of A5083-H32 aluminum alloy and performed microscopic morphology, surface topography, 3D surface topography, 2D roughness profiles, surface residual stress, and microhardness characterization analyses by changing the jet impact angle and abrasive mesh size. In 2017, Natarajan and Pradeep (2017) analyzed the influence of water jet pressure (100 MPa, 125 MPa, and 150 MPa) and jet impact angle (70°, 80°, and 90°) on the output parameters of jet cutting of different thicknesses of AA5083-H32 aluminum alloy. Niranjan et al. (2018) studied the effects of dynamic process parameters such as water pressure (100 MPa, 200 MPa, and 300 MPa), traverse speed, and abrasive mass flow rate on the penetration depth and surface topography of high-strength AZ91 magnesium alloy (Natarajan & Pradeep, 2017). Cai et al. (2019) extensively discussed the effects of factors such as abrasive water pressure (50 MPa, 80 MPa, 110 MPa, and 140 MPa), abrasive water standoff distance (4 mm, 8 mm, 12 mm, and 16 mm) on perforation length, maximum perforation diameter, shale mass loss, perforation velocity, effective perforation diameter, and other evaluation indicators. Zhao et al. (2023) constructed a finite AWJ cutting model using the SPH method. Vikas and Srinivas (2020) examined the response of output variables by setting different pressures (100 MPa, 200 MPa, and 300 MPa) and nozzle distances (1 mm, 2 mm, and 3 mm) and analyzing them using scanning electron microscopy. Tian et al. (2021) conducted numerical simulation on the working conditions of different nozzle types, nozzle lengths, and cone angle angles, and developed efficient and high cutting-effect nozzles. Demiral et al. (2022) studied the damage characteristics of composite material plates under different AWJ particle velocities (300 m/s-600 m/s). Gunamgari and Kharub (2022) studied the response of output variables to different AWJ particle velocities (130 mm/min and 259 mm/min) and nozzle distances (3 mm and 4 mm).

The existing research indicates that there have been numerous numerical simulations and experimental studies on AWJ cutting technology. Corresponding conclusions have been drawn regarding the inherent effect mechanisms of AWJ on target materials and the influence of process parameters in the cutting process. However, previous studies mainly focused on the effects of individual variables such as pump pressure, displacement, jet velocity, or nozzle diameter using controlled variable methods. There has been limited research on the interaction among pump pressure, displacement, and nozzle diameter in the AWJ cutting process, as well as the optimization of nozzle structural parameters. Therefore, this paper established Fluent models with different nozzle shapes and SPH-FEM coupled models for simulation calculations. By combining theoretical analysis and numerical simulations, this paper attempted to investigate the effects of nozzle parameters and process parameters on the cutting efficiency of AWJ.

Firstly, we conducted CFD numerical research on six different nozzle shapes. We then selected a conical nozzle for comparative analysis, with the purpose of studying the flow structure with different duct lengths and tapers. Subsequently, we discussed the effects of pump pressure, displacement, and nozzle diameter on cutting efficiency. Finally, an infinite SPH model was established for AWJ cutting, with cutting depth and volume as evaluation criteria for analysis.

2. ESEARCH METHODS

2.1 Coupled SPH-FEM Method

As shown in Fig. 1, Smoothed Particle Hydrodynamics (SPH) is a typical meshless computational method in which the continuous fluid or solid is described by interacting discrete particles (Hu et al., 2015; Yang et al., 2019). The core idea is to represent the fluid or solid as a collection of interacting particles,

Traditional grid-based   **SPH grid-based**
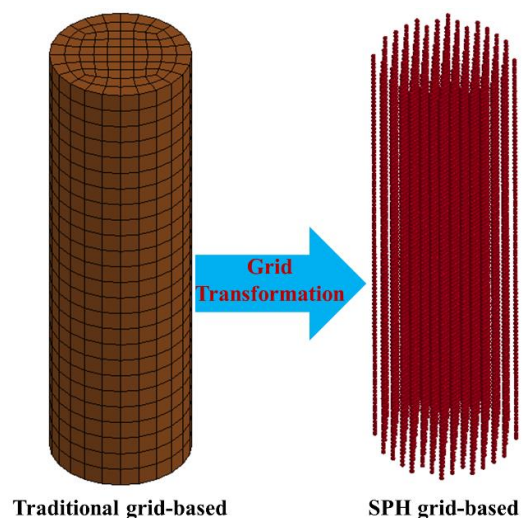
Fig. 1 Schematic diagram of SPH discretized particle

each carrying a different physical quality. The mechanical behavior of the entire fluid system can be obtained by solving the dynamic equations of the particle group (Zhao

et al., 2010). SPH has been widely adopted and applied in areas such as impact deformation and fluid-structure coupling because of its advantages in handling large deformation, stress localization and other issues.

The core idea of the SPH method is to represent the problem domain in the form of particles. In the computation process, particles need to be approximated at each step based on the current support domain with arbitrary distribution of particles, allowing the SPH method to handle large deformation. The particle approximation method is then used to further approximate the governing equations using particles.

The partial differential equations for discrete sample points are approximated using the reproducing kernel function (Chu et al., 2018). The equations are then directly transformed into integral equations by employing the reproducing kernel interpolation. This is achieved by using the cylindrical scatter interpolation method at the discrete points to calculate the unknown function values at other nodes. The integral values of the functions can be obtained by integrating discrete nodes. In the discrete form, it can be written as:

$$f_h(x) = \sum_{n=1}^{N} f(x_a) W(x - x_a, h) V_a \qquad (1)$$

where N represents the total number of nodes in the entire domain, $W(x - x_a, h)$ is the kernel function located at node x_a, and V_a is the statistical volume associated with node a. In the SPH meshless method, it is assumed that the nodes or particles are distributed in a continuous and relatively regular manner. V_a in Eq. (1) is calculated using random simulation method. The formula for density function can be expressed as:

$$n(x) = \sum_{n=1}^{N} \delta(x - x_a) \qquad (2)$$

where $x_a (a = 1,2 \dots N)$ represents the vector of N nodes distributed in the domain, and δ is the Dirac Delta function. According to the definition of the reproducing kernel function, $[n(x)]$ can be written as:

$$[n(x)] = \sum_{b=1}^{N} \int_B \delta(x - x_a) W(x - x', h) dx' \qquad (3)$$

Taking into account the properties of the Dirac Delta function, we have:

$$\int_B \delta(x - x_a) dx_a = \begin{cases} 1 & x \in B \\ 0 & x \notin B \end{cases} \qquad (4)$$

where B is a symmetric base function centered at x. Therefore, Eq. (3) can be simplified as:

$$V(x)^{-1} = [n(x)] = \sum_{b-1}^{N} W(x - x_b, h) \qquad (5)$$

Similarly, using the concept of shape function in finite elements, we can also obtain SPH function. The discretization of nodes in Eq. (1) can be expressed as:

$$f_h(x_a') = \sum_{b-1}^{N} \varphi_b(x_a) f(x_b) \qquad (6)$$

where $\varphi_b(x_a) = W(x_a - x_b, h) V_b$ represents the shape function of the SPH method. The approximate function values in SPH are not equal to the function values at the unknown function nodes, that is, $f_h(x_a) \neq f(x_a)$. At the same time, the shape function does not satisfy the properties of shape function in finite element method.

$$\varphi_b(x_a) \neq \delta_{ba}, \qquad \delta = \begin{cases} 1, & b = a \\ 0, & b \neq a \end{cases} \qquad (7)$$

The discrete form of the SPH method satisfies the consistency condition, and standard interpolation can be achieved only if the following conditions are satisfied.

$$\sum_{b=1}^{N} \varphi_b(x_a) \cong 1; \sum_{b=1}^{N} x_i^{(b)} \varphi_b(x_a) \cong x_i^{(a)} \qquad (8)$$

where $x_i^{(b)} (i = 1,2,3 \dots)$ represents the ith coordinate of node b. When boundary conditions are not considered and there are sufficient nodes, the analytical structure of the SPH method is relatively ideal (Murugesh & Scattergood, 1990).

In summary, while the meshless particle method has certain advantages in dealing with collision and large deformation, its computational efficiency has always been a significant concern (Antuono et al., 2012; Crespo et al., 2015). In this study, based on the traditional SPH numerical model, we simplified the finite SPH particles into an infinite particle model, as shown in Fig. 2. Additionally, we defined the neighborhood search range for SPH, where particles that leave this range automatically become inactive. As a result, the model can continuously generate water and abrasive particles,
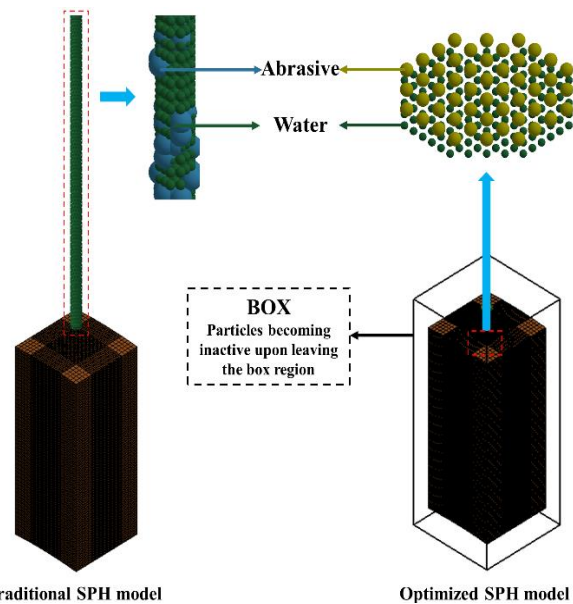
Fig. 2 Schematic diagram of SPH model optimization
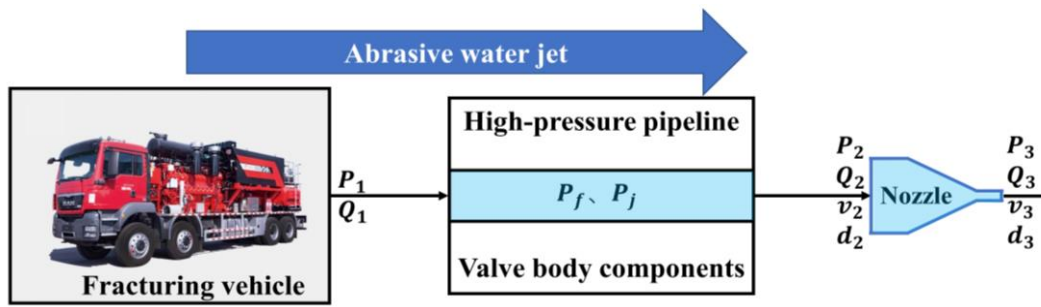
Fig. 3 Schematic diagram of AWJ cutting process

meeting the simulation requirements and improving efficiency while saving a significant amount of computational time.

2.2 The Relationship Among Coupled Pressure, Displacement and Nozzle Diameter

Figure 3 illustrates the process of AWJ cutting. There are three interrelated and mutually influential crucial parameters in AWJ machining, namely pump pressure, displacement, and nozzle diameter. Among them, pump pressure serves as the driving force for propelling the fluid particles, and the higher the pump pressure, the greater the velocity of ejected abrasive particles. Displacement refers to the volume of the abrasive and air mixture pumped per unit time, and the larger the displacement, the more the ejected abrasive particles. Thus, higher pump pressure and displacement indicate a greater energy possessed by the AWJ, resulting in higher cutting efficiency. Nozzle diameter is an important factor that limits the energy of the fluid. Using a nozzle with a larger diameter for cutting requires a power source that can provide a significant displacement and power to achieve optimal cutting efficiency. Generally, at a fixed nozzle diameter, displacement will increase with pump pressure. Similarly, when pump pressure is fixed, displacement will also increase with nozzle diameter. To conclude, it is not feasible to study the pump pressure, displacement, and nozzle diameter as independent variables using a controlled variable approach in the AWJ cutting process. Instead, a coupled research method is required to obtain conclusions that are closer to real-world scenarios.

2.2.1 Pressure Pump

Fracturing pump is a common power source for AWJ cutting process, and its performance parameters mainly include pump pressure, displacement, and power, which are of great importance to measuring the performance of the fracturing pump. Among them, pressure refers to the pressure output by the fracturing pump, a critical parameter to ensure that the fluid can overcome formation resistance and be injected smoothly, displacement refers to the flow rate output by the fracturing pump, an important factor affecting fluid jet velocity and cutting efficiency and power represents the energy required for the operation of the fracturing pump that directly affects the operational efficiency and cost of the fracturing pump. Therefore, understanding the relationship between pump pressure, displacement, and power is of significant

importance for the rational selection and use of fracturing pumps.

Based on experience and experimental results, pump pressure, displacement, and power are associated to a certain extent. Specifically, pump pressure and displacement are directly proportional to power demand, which means that as pump pressure or displacement increases, more power is required to drive the fracturing pump. At the same time, when power remains constant, increasing pump pressure leads to a decrease in displacement, and increasing displacement also leads to a decrease in pump pressure. These relationships can be expressed using the following formula:

$$N = P_1 \times \frac{Q_1}{60} \times 10^3 \tag{9}$$

where N represents the power of the fracturing pump in kilowatt; P_1 represents the pump pressure of the fracturing pump in megapascal; Q_1 represents the displacement of the fracturing pump in cubic meter per minute.

2.2.2 Pump Pressure and Displacement

Pump pressure is the initial pressure of a fracturing vehicle, equal to jet pressure (nozzle pressure drop) plus frictional pressure loss along the path and local pressure loss. It can be calculated by:

$$P_1 = P_2 + P_f + P_j \tag{10}$$

where P_1 represents pump pressure; P_2 represents jet pressure; P_f represents frictional pressure loss along the path; P_j represents local pressure loss.

At a constant flow rate, the frictional pressure loss along the path and the local pressure loss remain relatively constant. The pump pressure P_1 is positively correlated with the jet pressure P_2. The higher the threshold pressure of the target, the higher the required jet pressure and pump pressure. However, the pump pressure cannot increase indefinitely and should not exceed the rated pressure of the pump. Plunger pumps are commonly used as the pump source, which are positive displacement pumps with a constant flow rate. The pressure provided by the pump is related to the pressure drop in the system. Therefore, the rated pressure of the pump is generally higher than the sum of the pressure drops in the system.

Within the realm of AWJ cutting, high-pressure pipelines and valve components play crucial roles as integral structural elements. Abrasive slurry will

inevitably encounters resistance losses when flowing through high-pressure pipelines. Similarly, when water flows through the valves, there will be abrupt changes in the cross-sectional area and alterations in the flow direction, resulting in localized resistance losses.

The magnitude of resistance losses along the pipeline can be determined by:

$$P_f = \frac{8\rho\lambda L Q^2}{\pi^2 D^5} \tag{11}$$

where D is the diameter of the pipeline; Q is the flow rate of the system; L is the length of the pipeline; ρ is the density of the fluid; λ is frictional resistance coefficient.

The magnitude of localized resistance losses can be determined by:

$$h_j = 8\lambda \frac{l_0 Q^2}{\pi^2 d^3 g} \tag{12}$$

where l_0 represents the equivalent length of the pipe; P_j denotes the local resistance at the valve; ρ represents the density of the fluid; λ signifies the resistance coefficient along the path; v represents average fluid velocity; Q denotes corresponding flow rate.

As can be clearly seen from Eqs. (11) and (12), with the decrease in the inner diameter of a high-pressure pipeline, both fluid velocity and pressure loss increase. Therefore, it is not advisable to choose a high-pressure pipeline with a small inner diameter. However, the inner diameter of a high-pressure pipeline should also not be too large. In the case of too large diameter, the velocity of the abrasive fluid will decrease. When the velocity falls below the critical settling velocity, sedimentation will occur, thus affecting the operation stability of water jet and potentially resulting in blockage and potential hazards in the high-pressure pipeline. The resistance coefficient along the path is mainly determined by the brand of pipeline. Once the system pipeline brand and inner diameter are determined, the system's flow rate becomes a factor determining the resistance loss along the path. Both the resistance loss along the path and the local resistance loss are directly proportional to the square of the flow rate.

2.2.3 Nozzle Diameter

The process of using high-pressure AWJ to cut workpieces by forming a water jet through a nozzle can be deduced through theoretical formulas to obtain relevant parameters. The theoretical derivation of the three main parameters, namely jet pressure, jet flow rate, and jet velocity, are given as follows. And relevant conclusions are drawn accordingly.

By applying the Bernoulli's equation between two points inside and outside the exit section of a continuous water jet nozzle, we can obtain

$$P_2 + \frac{1}{2}\rho_2 v_2^2 = P_3 + \frac{1}{2}\rho_3 v_3^2 \tag{13}$$

where: P_2 and P_3 represent the static pressures inside and outside the nozzle, respectively; v_2 and v_3 represent the average fluid velocities inside and outside the nozzle, respectively.

By applying the continuity equation between the two points, we can obtain

$$\rho_2 v_2 A_2 = \rho_3 v_3 A_3 \tag{14}$$

Assuming the nozzle exit is in the form of a circular pipe, $A = \pi \frac{d^2}{4}$, and assuming $\rho_2 = \rho_3$, we can deduce the following equation from the two equations mentioned above:

$$v_3 = \sqrt{\frac{2(P_2 - P_3)}{\rho\left[1 - \left(\frac{d_3}{d_2}\right)^4\right]}} \tag{15}$$

where d_2 and d_3 are the diameters of the pipe and the nozzle, respectively.

Since $p_2 \gg p_3$, $\left(\frac{d_3}{d_2}\right)^4 \ll 1$, we can derive the formula for jet velocity as:

$$v_3 = \sqrt{\frac{2P_2}{\rho}} \tag{16}$$

Given the jet velocity, we can obtain the flow rate by using the equation $q = v \cdot A$, which means the flow rate is equal to the exit velocity multiplied by the nozzle cross-sectional area.

$$Q_2 = \frac{\pi \cdot d_3^2}{4} \cdot v_3 = \pi \cdot d_3^2 \cdot \sqrt{\frac{P_2}{8\rho}} \tag{17}$$

Similarly, we can derive the equation

$$d_3^2 = \frac{Q_2}{\pi u_f}\sqrt{\frac{8\rho}{P_2}} \tag{18}$$

$$P_2 = \frac{8\rho Q_2^2}{\pi^2 d_3^4 u_f^2} \tag{19}$$

2.3 Numerical Simulation Model

The cutting well used in the experiment had a hollow cylindrical steel pipe with an inner diameter of 200 mm, an outer diameter of 400 mm, and a height of 800 mm. It was very difficult to perform cutting simulation calculation because of long cutting time and large size of the workpiece used. Therefore, a section of the central well with a dimension of 40 mm × 40 mm × 100 mm was taken as the scope for simulation calculation, as shown in Fig. 4, where the abrasive particles, the water particles and the 42-CrMo well are respectively marked in yellow, green and brown.

The 42-CrMo material is modeled using the Johnson-Cook constitutive model, with specific parameters detailed in Table 1. The abrasive particles are represented by 80-mesh garnet and modeled using the Elastic constitutive model; liquid water is described using the Null constitutive model, with material parameters provided in Table 2.

Considering the long computation time of the model and the requirement for computational accuracy, the mesh

Table 1 Parameters of constitutive model for 42-CrMo

Mass density	Shear modulus	Young's Modulus	Poisson's ratio
7.896e-06	81.8	185	0.313
Strength of extension	Yield strength	Specific heat	D1
1080	930	460	-0.8000000
D2	D3	D4	D5
2.01	-0.5	2.000e-04	0.61

Table 2 Parameters of constitutive model for water and abrasive

	Mass density	Young's modulus.	Poisson's ratio.
Water	1000kg/m³	-	-
Abrasive	4120 kg/m³	78GPa	0.3
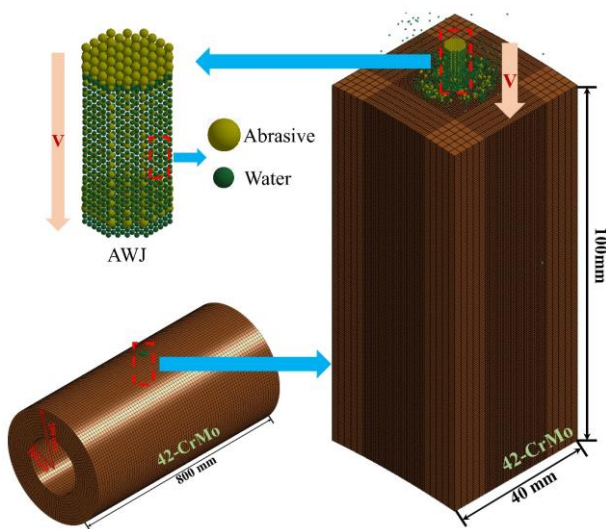
Fig. 4 Numerical model of AWJ cutting of wellbore

division of the model was mainly divided into two parts, namely the central part with a mesh size of 0.5 mm and the remaining parts with a mesh size of 1 mm. The model consisted of a total of 523,633 points, 500,000 solid elements, and 208 SPH particles.

The erosion node-surface contact method was adopted to establish the contacts between the abrasive particles and the well, as well as between the water particles and the well. Automatic contact between abrasive particles and water particles was achieved using SPH particles. The functionality to exclude deactivated particles was enabled to ensure that particles were deactivated and would not get involved in calculations after leaving the box range, reducing computational load. An infinite SPH particle model was employed in this experiment, and abrasive and water particles were continuously generated and the well was cut in the calculation process.

The basic assumptions of the model are described as follows: (1) The model flow field only contains abrasive particles and water particles. (2) The effects of air and gravity on the model are neglected. (3) There is no mass exchange between abrasive particles and water particles. (4) The influence of temperature changes on the fluid jet is neglected.

3. RESULTS AND DISCUSSION

Abrasive water jet cutting is one of the most widely applied and matured techniques in the field. The cutting efficiency of AWJ cutting is closely related to nozzle geometry, pump pressure, flow rate, abrasive concentration, standoff distance, and nozzle diameter. Therefore, this section focuses on simulating and calculating these parameters. The impact of various process parameters on AWJ cutting was studied by evaluating the length of the jet core region, cutting depth, and cutting volume as criteria.

3.1 Model Validation

42-CrMo steel, as a high-strength and high-toughness material, exhibits high fatigue limit strength and resistance to multiple impact loads after quenching and tempering treatment. Research on abrasive waterjet cutting of this type of material aims to optimize cutting parameters and improve cutting efficiency and quality, which is of great importance to the development of actual rescue and emergency operations.

Soori et al. (2023) studied the abrasive jet cutting of Ti6Al4V titanium alloy and used the SPH computational method to simulate the abrasive jet and the workpiece. In this study, experiments were also conducted to demonstrate the feasibility of the SPH numerical simulation method.

Previous studies have shown that pure water cutting of 42-CrMo steel causes minimal damage to the material, while the addition of abrasives significantly affects the integrity of the steel. In this section, three different cutting models, namely pure water cutting, pure abrasive cutting, and AWJ cutting, were established and validated, as shown in Fig. 5, where the exit velocity of the nozzle was V=290 m/s, the nozzle diameter was D=5 mm, simulation calculation time was t=1 ms, and the abrasive concentration was 25%.

(a) Pure water cutting model   (b) Abrasive Cutting   (c)Mixed Cutting
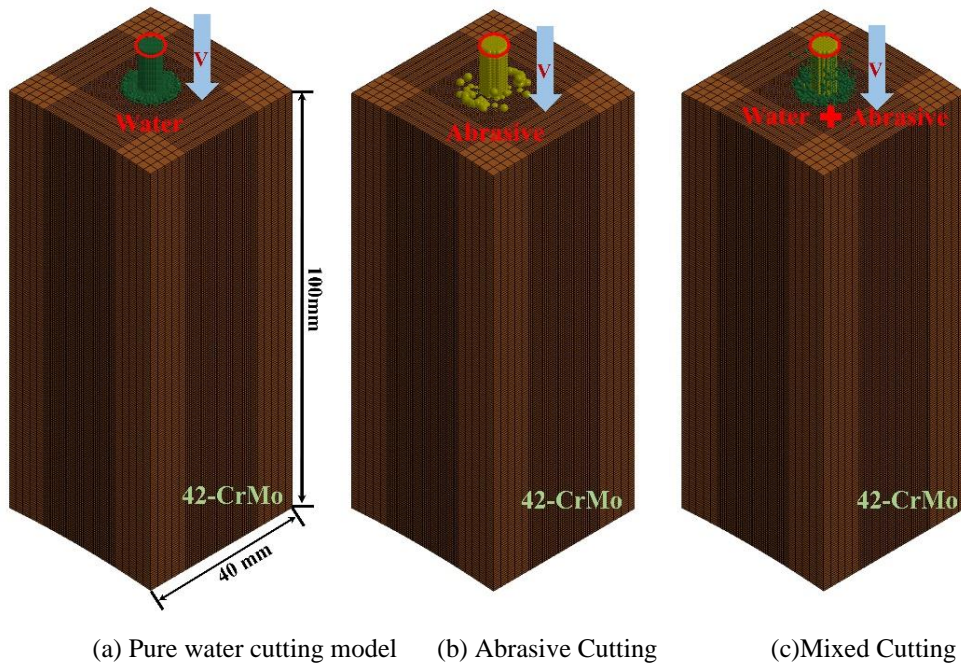
Fig. 5 Validation model diagram for 42-CrMo material

(a)   (b)   (c)
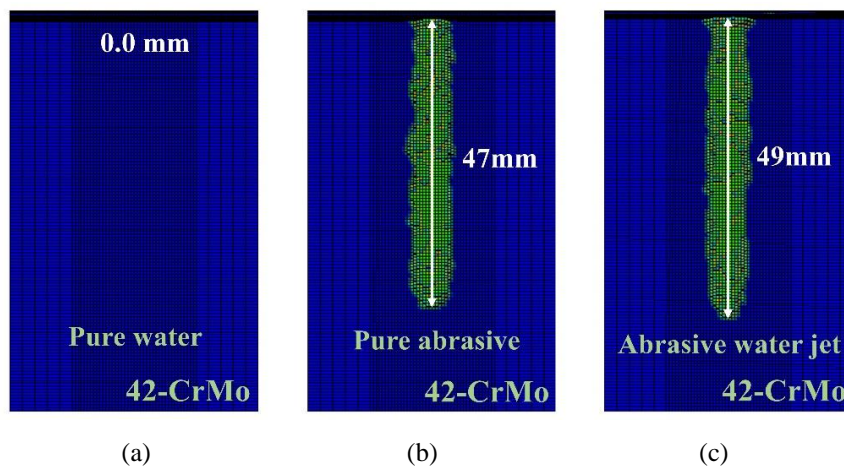
Fig. 6 Cloud map of cutting depth verification model

Figure 6 displays the cutting depths for different cutting methods. As shown in the Figure, the cutting depths for pure water jet, pure abrasive and AWJ were 0 mm, 47 mm and 49 mm, respectively.

Figure 7 shows the variation of cutting depth over time for three different cutting methods. The results showed: (1) Pure water jet cutting showed weak cutting force and could not reach the critical failure strength of the steel, thus causing minimal damage to the wellbore; (2) The cutting ability of abrasive particles was significantly stronger than that of water particles, but it could can cause noticeable damage to the wellbore; (3) The cutting depth of AWJ cutting was greater than that of pure abrasive cutting, indicating that water also played a certain facilitating role in the cutting process.

Therefore, the calculated results of the verification model aligned with the actual situation, thus demonstrating the rationality of using the SPH model in the study on the influence of AWJ working parameters on wellbore cutting. Nozzle Optimization

Figure 8 depicts the structural diagram of a jet. The AWJ is divided into four stages as it is ejected from the nozzle into the air, namely the initial jet core region, the transitional section where jet velocity slightly decreases and expands, the fundamental section where jet velocity gradually decreases, and the dissipation section where it merges with the surrounding air. Undoubtedly, high-speed concentrated jet in the initial stage was the preferred choice for cutting. The cutting depth and quality was determined by the velocity of the jet core region and the length of the constant velocity core region. The geometric structure of the nozzle was one of the important parameters that affect the length of the jet core region. A well-designed nozzle shape could help to reduce energy losses in the jetting process, thereby improving cutting efficiency.
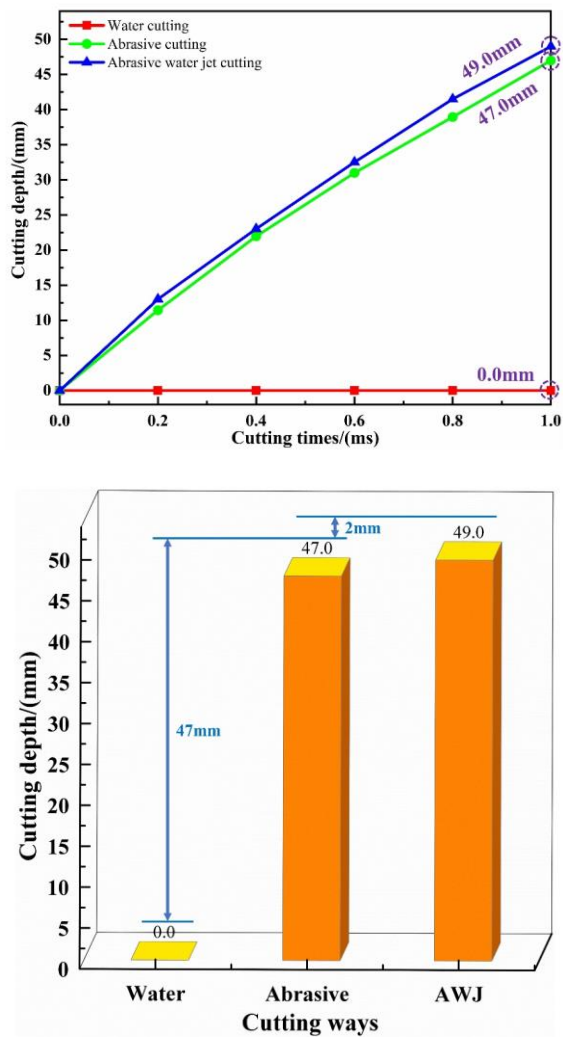
Fig. 7 Curve of cutting depth variation over time
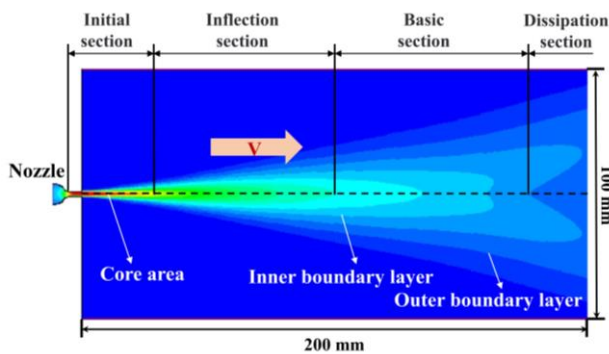
Fig. 8 Diagram of water jet structure model

3.1.1 Optimization of Nozzle Geometry

In this section, the internal and external flow fields of six different nozzle shapes were simulated using Fluent software to investigate the effects of different nozzle geometries in the AWJ cutting process so as to further identify the optimal nozzle for AWJ cutting. The selected nozzle shapes included variable velocity, streamlined, conical, cylindrical, arc-shaped, and double-arc-shaped nozzles. All nozzles had a cylindrical outlet with a diameter of 4 mm and a conduit with a length of 8 mm. Figure 9 illustrates the two-dimensional structural diagrams of the six nozzles.

A two-dimensional flow field model with a dimension of 200 mm × 100 mm was established. All the nozzles were subjected to the same initial and boundary conditions. The inlet and outlet boundaries were set as pressure boundaries, with an inlet pressure of 20 MPa and an outlet pressure at atmospheric pressure. The wall surfaces were set as non-slip boundaries. Water was used as the flowing medium, with a density of 998.2 kg/m^3 and a viscosity of 0.001 Pa·s.

Before the model calculations, a mesh independence verification was conducted for different models' mesh densities. Six different mesh sizes were selected: 0.5, 1, 2, 3, 4, and 5 mm, with the corresponding number of mesh elements shown in Table 3. Fluid simulation calculations of the nozzle jet were performed for these mesh sizes, and the results are as follows.

The calculation results are shown in Fig. 10. The models with mesh sizes of 5 mm, 4 mm, 3 mm, and 2 mm show significant differences compared to the models with mesh sizes of 1 mm and 0.5 mm, while the results for the 1 mm and 0.5 mm mesh sizes are similar. Since the model with a 0.5 mm mesh size has 75.3% more mesh elements than the 1 mm model, the computational workload increases significantly. Therefore, selecting a 1 mm mesh size model achieves optimal computational efficiency while maintaining accuracy.

The velocity contour maps of six different nozzle geometries were compared, with the red isovelocity lines representing the isovelocities of the fundamental section, as shown in Fig. 11. The cylindrical nozzle was the only one among the six nozzles that did not have a converging section. Its jet diffusion is significantly larger than that of the other five nozzles, which indicates that whether there was a converging section at the nozzle inlet had a noticeable impact on the jet diffusion at the nozzle outlet. By comparing the velocity contour maps of the other nozzle types, we observed that the internal flow channel shape of the nozzle had a significant influence on jet diffusion and the length of the constant velocity core. The three nozzle shapes of variable velocity, streamlined, and conical exhibited longer lengths of constant velocity lines, while the cylindrical, arc-shaped, and double-arc-shaped nozzles had shorter lengths of constant velocity lines.

Table 3 Mesh element size and quantity

Mesh Size (mm)	Mesh Quantity	Difference from 0.5 mm Mesh Quantity
0.5	171318	0%
1	42282	75.3%
2	10694	93.7%
3	4929	97.1%
4	2664	98.4%
5	1783	99.0%
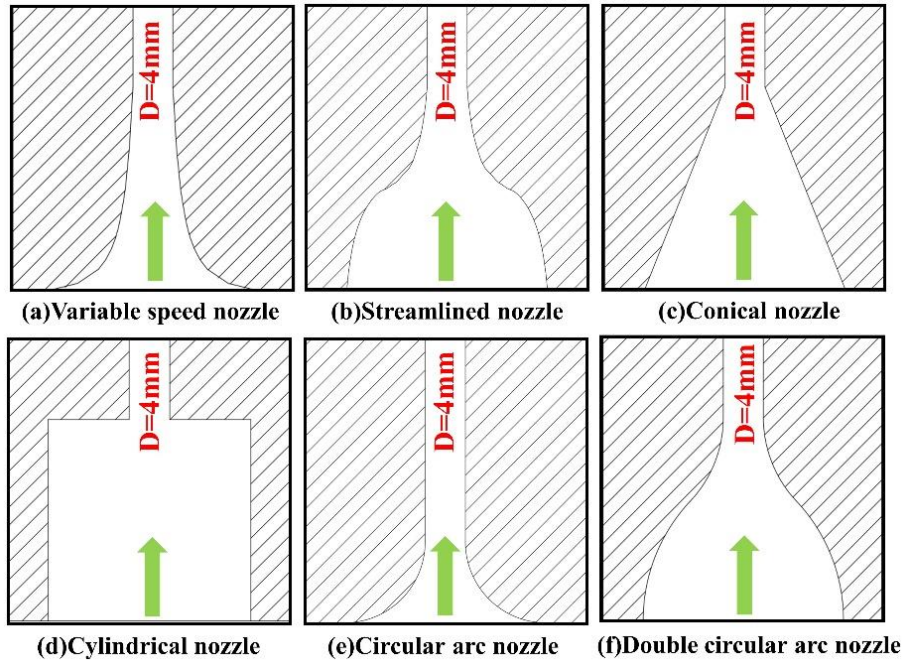
Fig. 9 Schematic diagram of the two-dimensional structure of the six nozzles
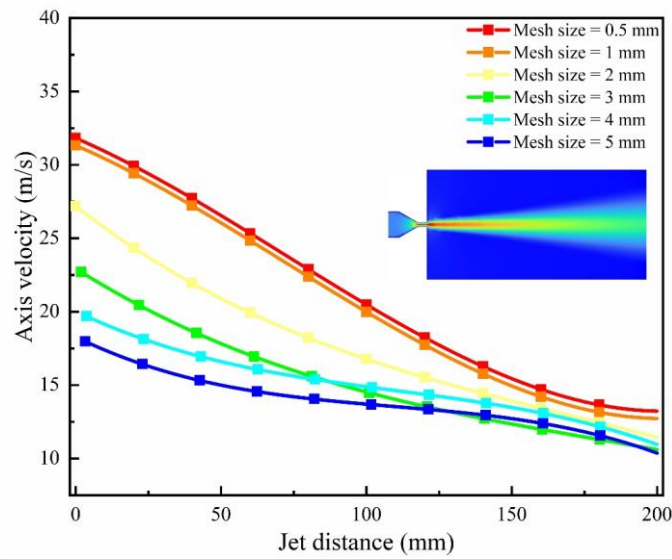
Fig. 10 Effect of mesh quantity on model results
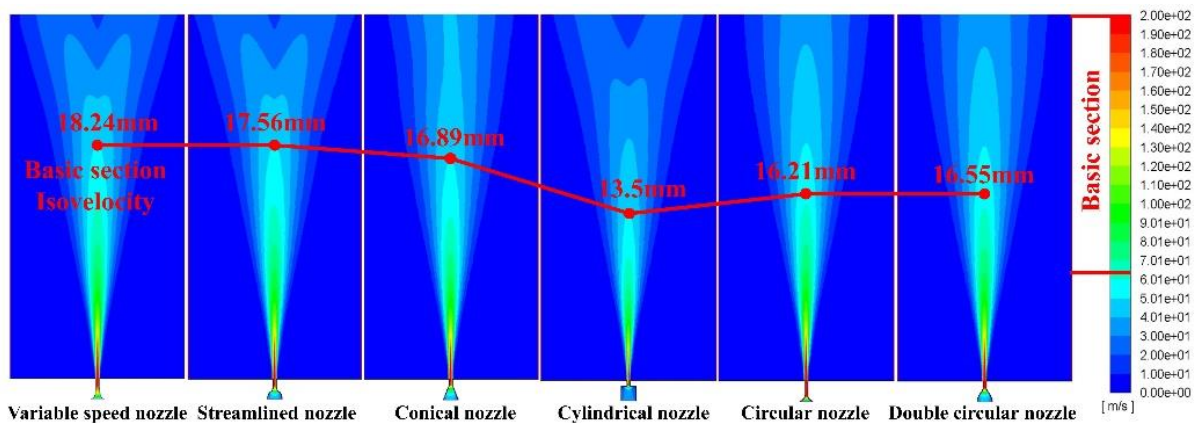
Fig. 11 Comparison of velocity distribution maps of jet in different nozzle geometries
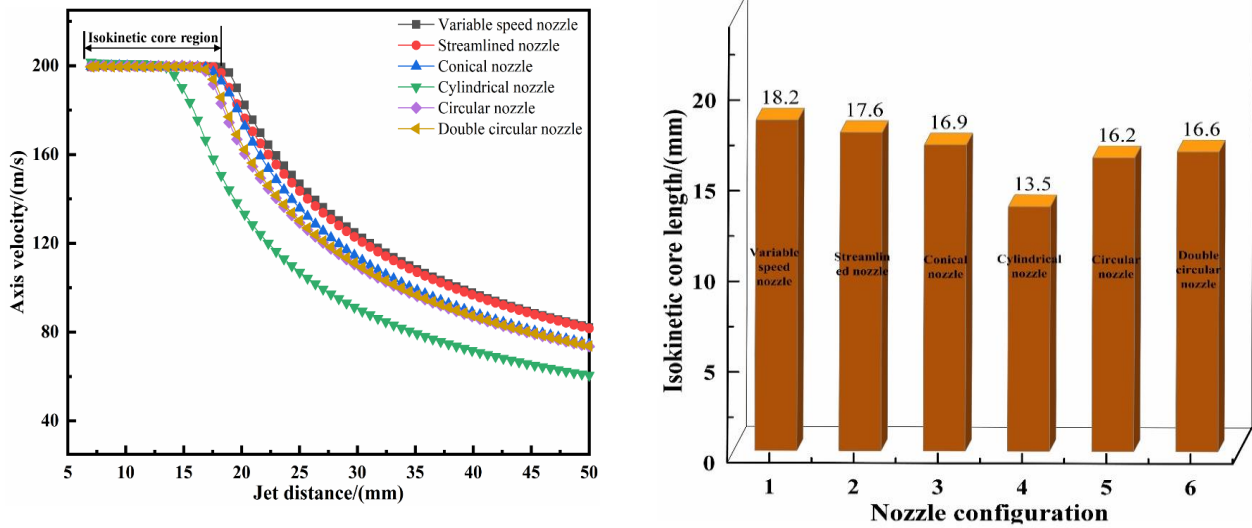
Fig. 12 Axial velocity distribution of jets with different nozzle types
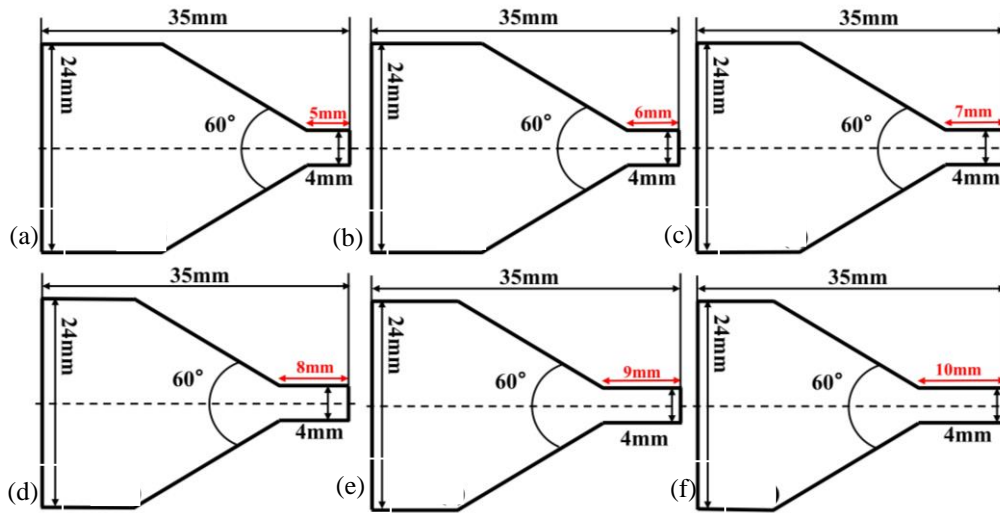
Fig. 13 Geometric structure of the nozzle with different duct lengths

The axial velocity distribution curves of different nozzle geometries were plotted based on the calculation results, as shown in Fig. 12. It can be seen from the Figure that following the ejection of the jet from the nozzle, there emerged a constant velocity core region where the axial velocity remained relatively constant. Outside the constant velocity core region, the velocity rapidly decreased till reaching a certain value. Following that, the decline rate of the velocity gradually decreased.

The research results indicated that among the six nozzle types, the variable velocity nozzle had the longest length of the constant velocity core, measuring 18.24 mm, followed by the streamlined nozzle with a length of 17.56 mm, the conical nozzle with a length of 16.89 mm, the cylindrical nozzle with a length of 13.5 mm, the arc-shaped nozzle with a length of 16.21 mm, and the double-arc-shaped nozzle with a length of 16.55 mm. The variable velocity, streamlined, and conical nozzles exhibited smaller jet diffusion and relatively slower velocity decay. However, the conical nozzle is preferred for AWJ cutting due to its simple structure, ease of manufacturing, and relatively excellent jetting performance in practice.

3.1.2 Optimization of Conical Nozzle

The cone angle and conduit length are two main parameters that affect the performance of a conical nozzle. In order to optimize these parameters, this section establishes various geometric models and corresponding fluid jet mathematical models using Fluent, and performs optimization calculations on the cone angle and conduit length to determine their impact on nozzle performance. By summarizing the results of calculations with different parameters, the optimal cone angle and conduit length for the conical nozzle are determined, aiming to maximize the cutting efficiency of AWJ.

The conduit length is an important geometric parameter in the geometric structure of a conical nozzle. The conduit length refers to the straight length of the conduit inside the AWJ nozzle. Different conduit lengths may lead to different flow characteristics inside the nozzle, affecting the distribution of pressure and velocity within the nozzle, thereby improving cutting quality and efficiency. As depicted in Fig. 13, a fluent model was established for six different conduit lengths (5 mm, 6
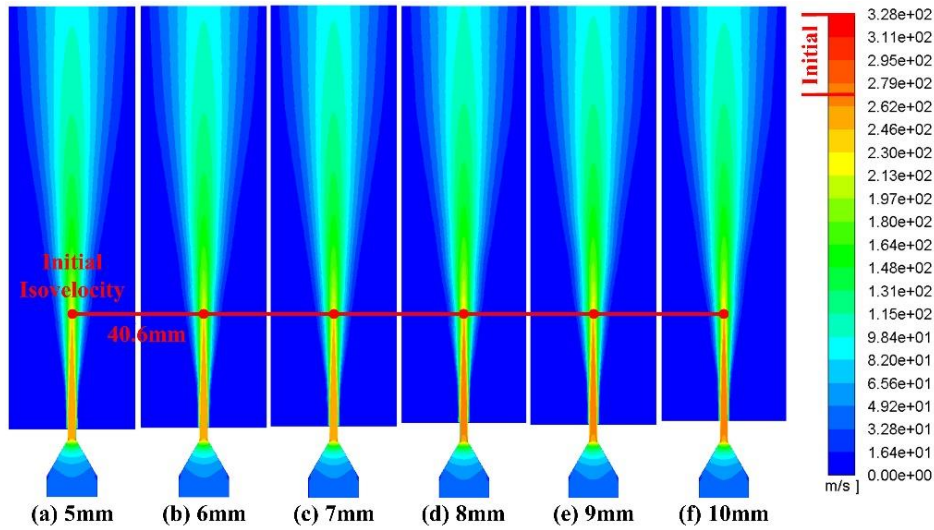
Fig. 14 Velocity distribution map of jets with nozzles of different lengths
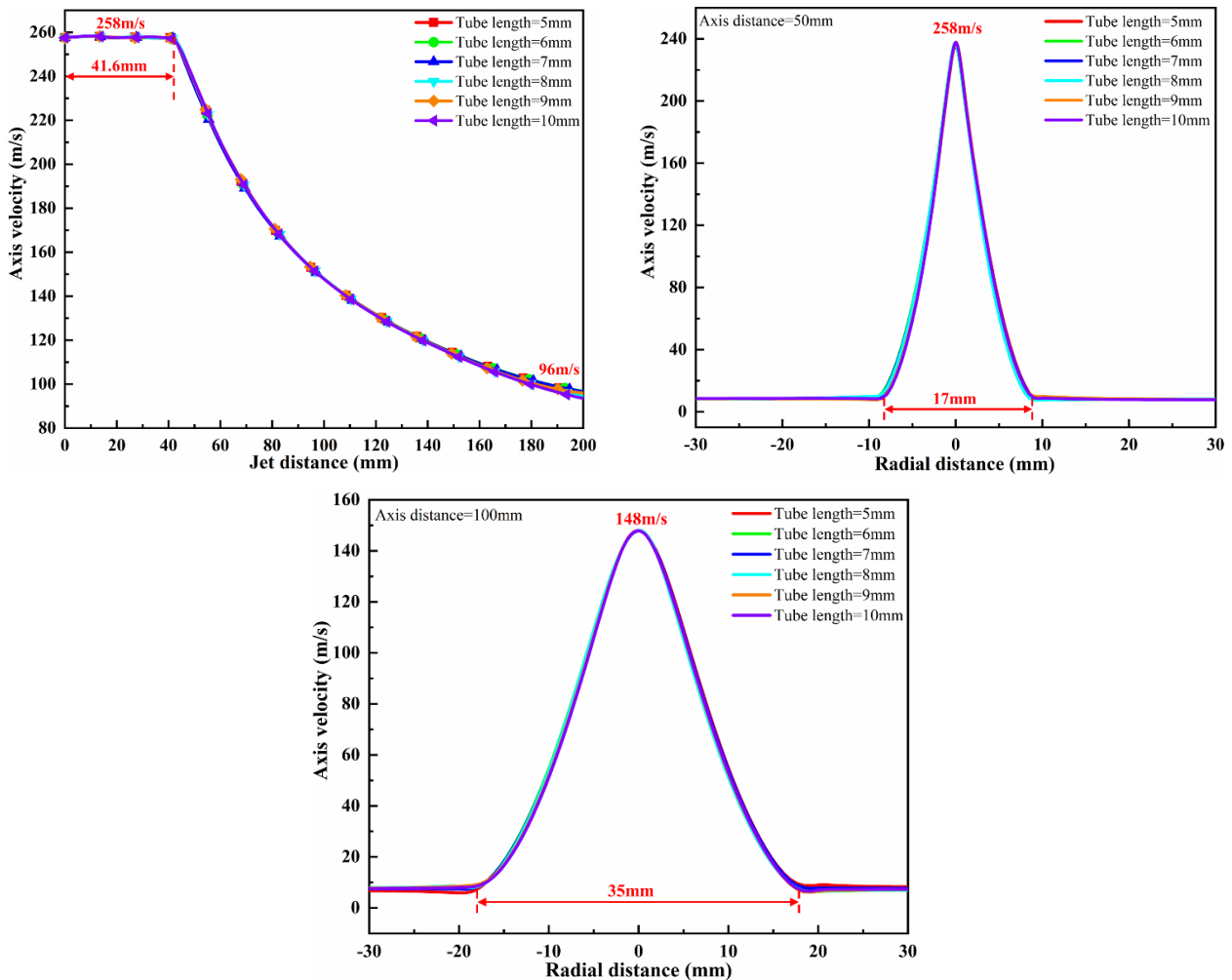
Fig. 15 Velocity profile of jets with nozzles of different duct lengths

mm, 7 mm, 8 mm, 9 mm, and 10 mm). The cone angle of the nozzle was fixed at 60°, and the overall length of the nozzle geometry remained constant at 35 mm. The boundary parameter conditions for the model were set as follows: The jet pressure was 40 MPa, fluid density was 1,200 kg/m³ and viscosity was 0.01 kg/m-s.

When the AWJ passes through the conduit, the variation in conduit length will affect the velocity and flow rate. The calculation results are shown in Figs. 14 and 15. By analyzing the axial velocity curve, we observed that

the velocity in the constant velocity core region inside the conduit was 258 m/s for different lengths, and the length of the constant velocity core region was 41.6 mm. In addition, the radial velocity curves at 50 mm and 100 mm in the axial direction were also essentially the same. While longer conduits may slightly reduce diffusion, the impact of conduit length on AWJ cutting was not significant for the conical nozzle. Therefore, when designing AWJ machining, we should prioritize other factors such as abrasive size, flow rate, and pressure. And in the design of conical nozzles, the length of conduit needs to be considered according to actual needs to achieve better machining results. In the manufacturing process, attention should also be paid to the manufacturing quality and material selection of the conduit to ensure its stability and reliability. Only by considering various factors comprehensively could the efficiency and accuracy of AWJ machining be improved.

Different taper angles will alter the distribution and velocity of internal flow within the nozzle, thereby affecting the collision effect between abrasive particles and the material being cut. Six geometric models with taper angles of 40°, 60°, 80°, 100°, 120°, and 140° were respectively established, as shown in Fig. 16. The boundary conditions of the models are as follows: jet pressure was 40 MPa, duct length was 8 mm, fluid density was 1,200 kg/m³ and viscosity was 0.01 kg/m-s.

When the AWJ passes through a conical nozzle, changes in the cone angle of the nozzle will affect the jet velocity. The velocity contour maps of nozzles with different cone angles were drawn based on the calculation results, as shown in Fig. 17. The position of the constant velocity lines revealed that the energy attenuation of the jet increased with the nozzle cone angle. The jet velocity was relatively high when the cone angles were 40°, 60°, and 80°, but when the cone angle reached 100°, the constant velocity lines showed a sudden downward trend, suggesting that the smaller the cone angle of the conical nozzle, the longer the constant velocity core of the jet.
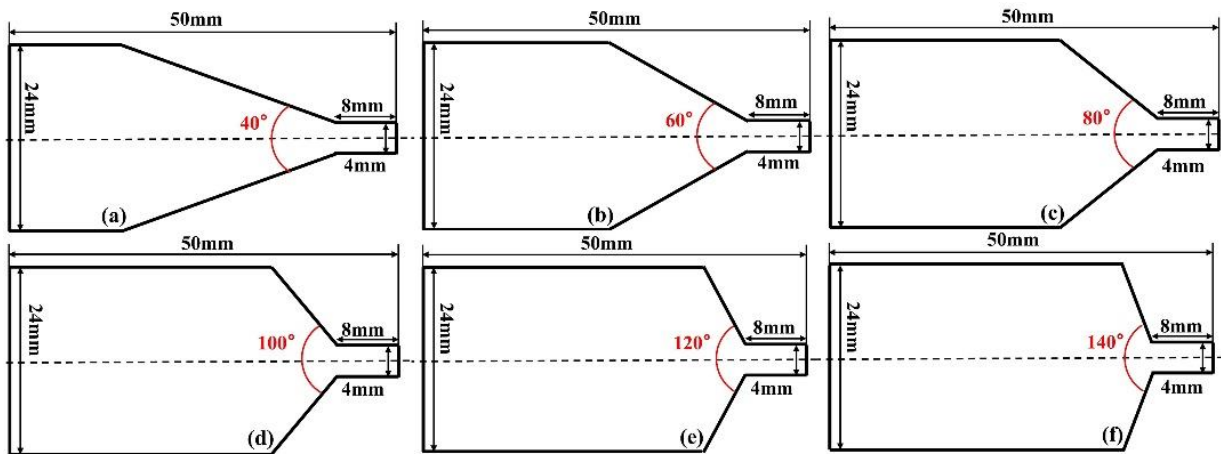
Fig. 16 Geometric structure of nozzle with different taper angles
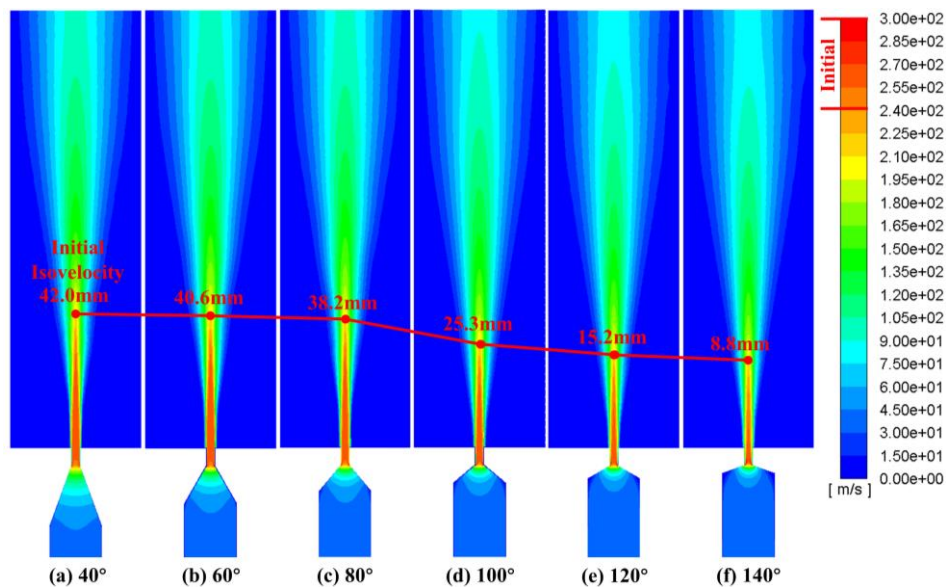
Fig. 17 Velocity distribution map of jets with the conical nozzle of different taper angles
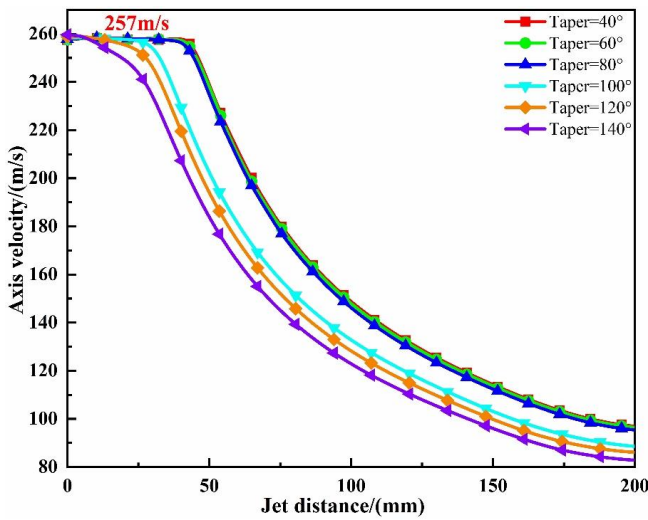
Fig. 18 Axial velocity profiles of jet flow in different conical nozzle tapers
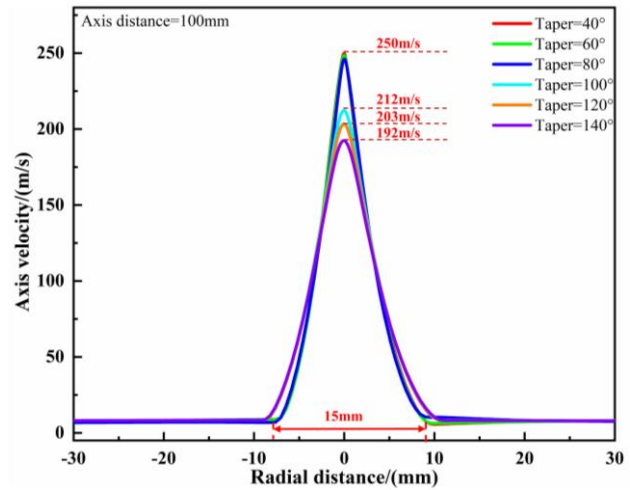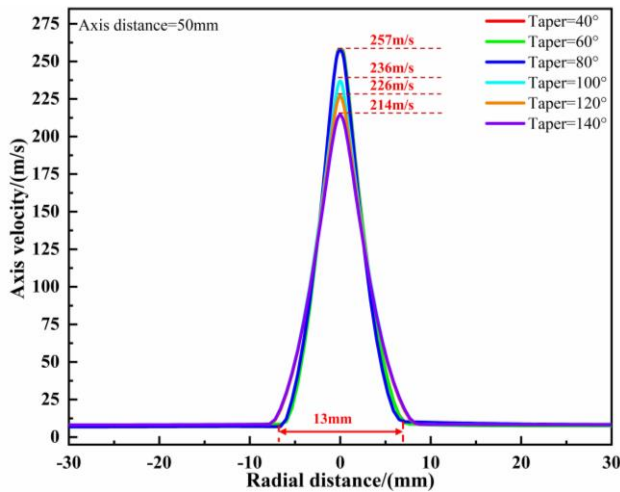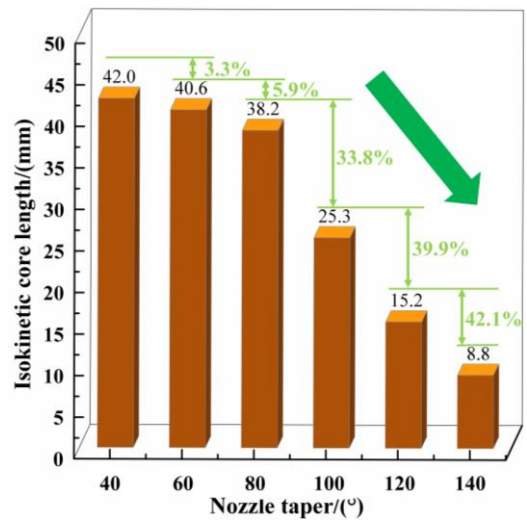
Fig. 19 Vertical velocity profiles of jet flow in different conical nozzle tapers

Based on the calculation data, the axial and radical velocity profiles of jet flow under different conical nozzle tapers were plotted, as shown in Figs. 18 and 19. As can be seen from the Figures, the larger the cone angle of the conical nozzle, the faster the energy attenuation of AWJ. The length of the constant velocity core zone was 42 mm, 40.6 mm, 38.2 mm, 25.3 mm and 8.8 mm respectively when the cone angle of the conical nozzle was 40°, 60°, 80°, 100°, and 120°. The attenuation rate reached a maximum of 33.8% when the nozzle cone angle was raised from 80° to 100°. In the radial direction, the axial velocities of the nozzle with cone angles of 40°, 60°, and 80° were basically the same. However, for cone angles larger than 80°, there was a significant decrease in axial velocity.

The results indicate that a smaller cone angle of the conical nozzle leads to higher jet velocities. Within the range of cone angles from 40° to 80°, the cutting efficiency is similar, and the energy loss is minimal.

3.1.3 Analysis of Blockage in Conical Nozzles

A Fluent-EDM coupled model with nozzle taper angles ranging from 40° to 120° was established, in which 10,000 fixed abrasive particles were generated in the flow channel, as shown in Fig.20. Except for the varying nozzle taper angles, all other parameters remained constant. The simulation calculated the number of particles passing through each conical nozzle within a fixed time period. A higher number of particles passing through indicates better flow efficiency of the nozzle in the abrasive jet process. The analysis results are as follows:
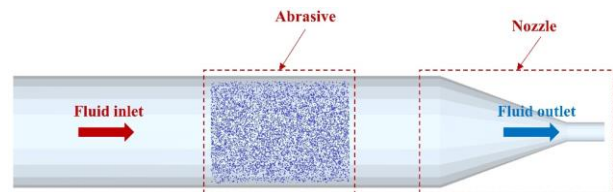
Fig. 20 Blockage model of the conical nozzle establishment
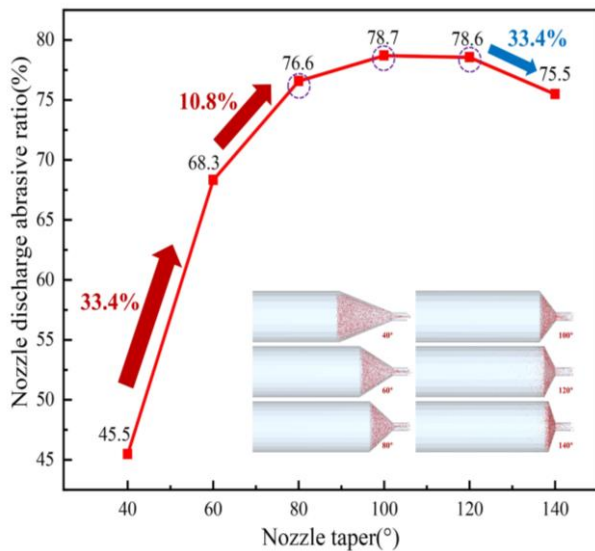
Fig. 21 Abrasive particle blockage simulation results for nozzles with different cone angles

As shown in Fig.21, for the nozzle with a 40° taper, 45.5% of the abrasive particles exited; for the 60° taper, 68.3% exited; for the 80° taper, 76.6% exited; for the 100° taper, 78.7% exited; for the 120° taper, 78.6% exited; and for the 140° taper, 75.5% exited. Among these, the 80° nozzle demonstrated the best particle flow efficiency, while the 40° nozzle experienced the most severe particle blockage.

In summary, considering both the jet velocity and particle blockage, the conical nozzle with an 80° taper provides the optimal performance. Therefore, when performing AWJ cutting, the taper of the conical nozzle needs to be properly sized. Based on a comprehensive consideration of the calculation results, it is recommended to use a conical nozzle with an 80° taper to achieve optimal jet velocity in the AWJ process while effectively avoiding

3.2 Comparison of Abrasive Concentration

Based on the model in Section 2.3, the number of water particles was kept constant, while the abrasive concentration was adjusted by changing the number of abrasive particles. Different SPH (Smoothed Particle Hydrodynamics) cutting models with varying abrasive concentrations were established, and numerical simulations were conducted to study the effect of abrasive concentration on cutting efficiency.

Abrasive concentration, an important parameter in abrasive water jet machining, reflects the proportion of abrasive particles in the jet per unit volume and affects the number of abrasive particles acting on the workpiece material per unit time. Under certain working conditions, the abrasive concentration ranged from 150 to 650 kg/m³, and the nozzle diameter was 4.5 mm. The discharge rates of the fracturing truck were 0.47 m³/min, 0.55 m³/min, and 0.64 m³/min, respectively. Simulation calculations under different working conditions were compared.
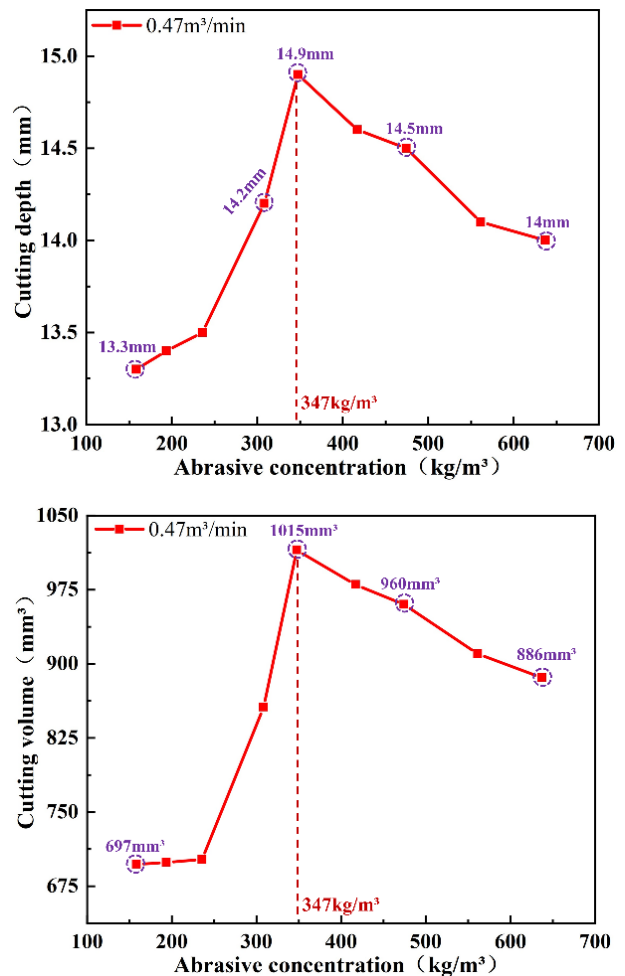
Fig. 22 Cutting depth and cutting volume curves at a discharge rate of 0.47 m³/min

The results indicated that in the process of cutting hard-to-machine materials, abrasive particles are the primary medium for material removal. Increasing the abrasive flow rate increased the cutting depth and the material removal capability of the abrasive water jet. However, interestingly, at a low abrasive flow rate, cutting depth increased with the flow rate, but decreased when the flow rate reached a certain value mainly because at high abrasive concentrations, the excessive number of abrasive particles per unit volume resulted in severe interference among the particles and thus significant energy loss. Figure 22 shows that at a discharge rate of 0.47 m³/min, the maximum cutting efficiency was achieved at an abrasive concentration of around 347 kg/m³. Figure 23 shows that at a discharge rate of 0.55 m³/min, the maximum cutting efficiency was achieved at an abrasive concentration of around 420 kg/m³. Figure 24 shows that at a discharge rate of 0.64 m³/min, the maximum cutting efficiency was achieved at an abrasive concentration of around 450 kg/m³. These results implied that in the abrasive jet cutting process, there was an optimal abrasive concentration for each set of working conditions when maximum cutting efficiency could be achieved. Additionally, with the increase of discharge rate, the optimal abrasive concentration for abrasive jet cutting increased.
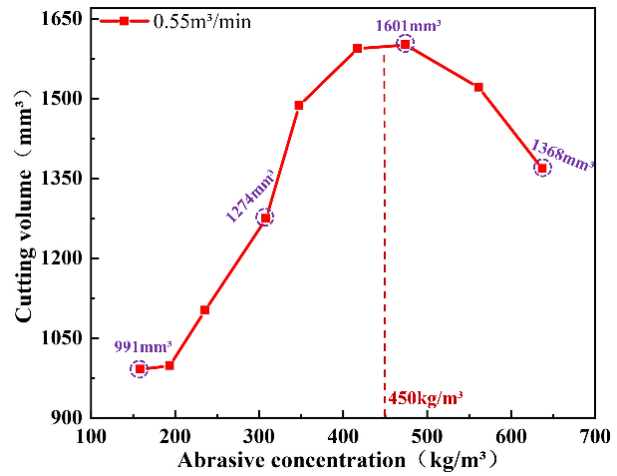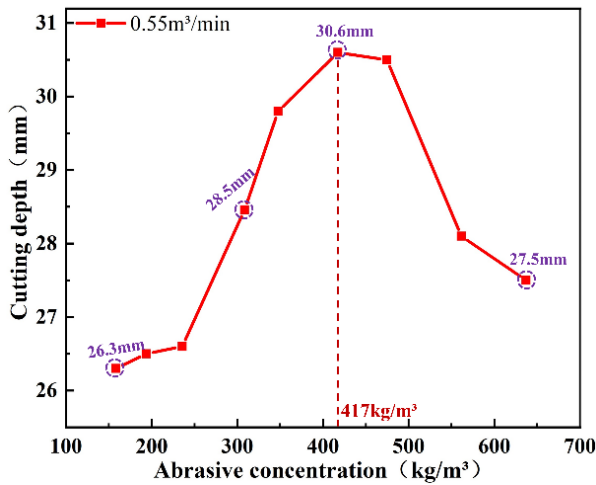
Fig. 23 Cutting depth and cutting volume curves at a discharge rate of 0.55 m³/min
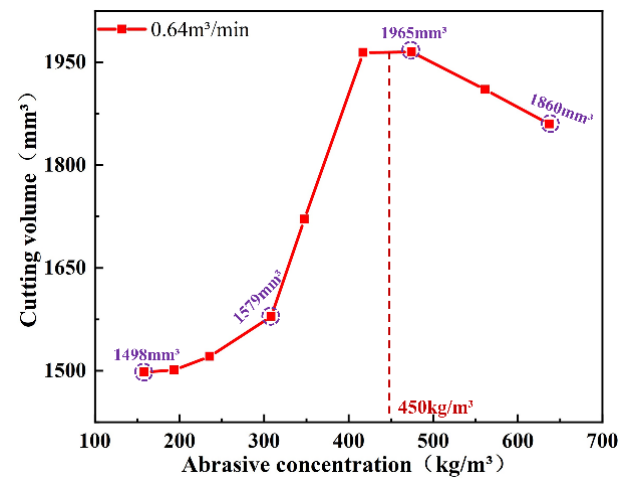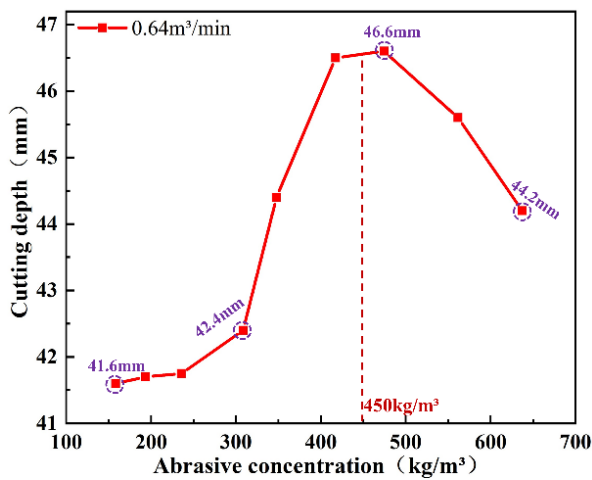
Fig. 24 Cutting depth and cutting volume curves at a discharge rate of 0.64 m³/min

Table 4 Parameters of different models of fracturing trucks

Fracturing vehicle model	Max pressure (MPa)	Max displacement (m³/min)	Max power (hp)
700	60	1.76	700
1800	61	1.82	1800
2300	88	2.6	2300

3.3 Different Models of Fracturing Vehicles

Based on the model in Section 2.3, a large number of orthogonal simulations will be conducted by varying the nozzle diameter and jet flow rate. To align more closely with practical work conditions, this section will compare the simulation results with the parameters of four different models of fracturing trucks. Through data analysis, we will clarify the relationship between the nozzle diameter for abrasive jet cutting of wellbores and the models of fracturing trucks, leading to the identification of underlying patterns.

Fracturing trucks serve as the power source for abrasive jets, and different models of fracturing trucks have varying maximum power, maximum pump pressure, and maximum discharge rates. In this section, we selected four different models of fracturing trucks, namely models 700, 1800, 2300, and 2500, as the subjects of our study. The relevant parameters are listed in Table 4. Using the coupling relationships among pump pressure, discharge rate, and nozzle diameter, we analyzed maximum cutting depth and maximum cutting volume that could be achieved by different models of fracturing trucks with different nozzle diameters.

As shown in Fig. 25, the nozzle diameter was 6 mm, the discharge rate was 1.13m³/min, and the pump pressure was 98 MPa. The cutting process at different times revealed that with the progression of the cutting time, the abrasive jet continuously damaged the workpiece. The cutting depth at 0.2 ms and 1.5 ms separately reached 13.5 mm and 97.5 mm.

Based on the calculation method, the cutting depth and cutting volume curves for the 700, 1300, 2300 and
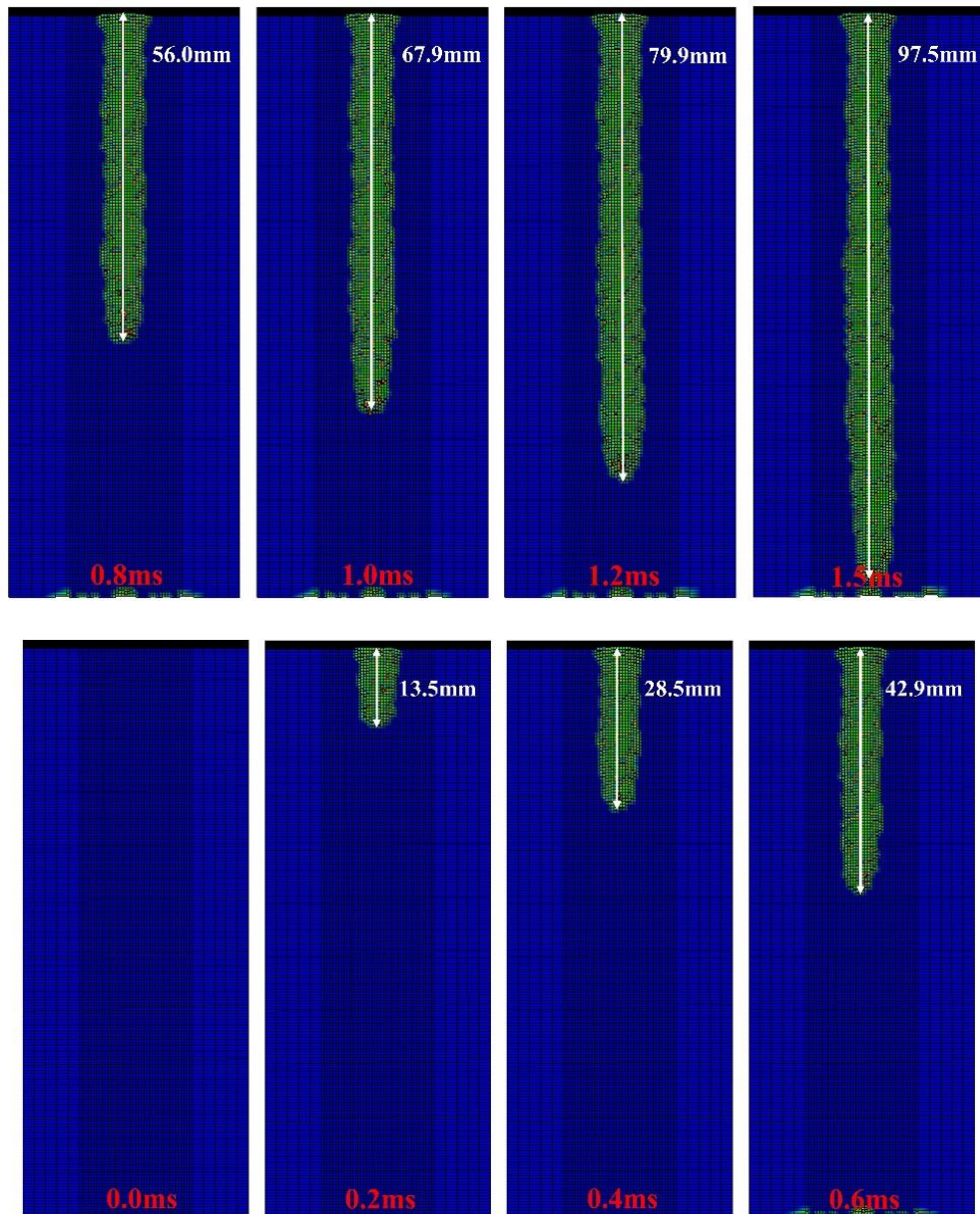
Fig. 25 Schematic diagram of steel damages at different cutting time

2500-type fracturing trucks under different nozzle diameters were plotted, as shown in Figs. 26, 27, 28 and 29. According to the pattern, with the increase of the nozzle diameter, cutting depth and cutting volume curves first increased and then decreased. The 700-type fracturing truck exhibited the highest cutting efficiency with a nozzle diameter of 4 mm, pump pressure of 55 MPa, discharge rate of 0.47 m³/min, and power of 527 KW; the 1800-type fracturing truck achieved the best cutting efficiency with the nozzle diameter of 4 mm-4.5 mm, pump pressure of 56 MPa, discharge rate of 0.57 m³/min, and power of 653 KW; the 2300-type fracturing truck achieved the best cutting efficiency with a nozzle diameter of 4.5 mm, pump pressure of 79 MPa, discharge rate of 0.68 m³/min, and power of 1,111 KW, and the 2500-type fracturing truck achieved the best cutting efficiency with the nozzle diameter of 4.5 mm-5 mm, pump pressure of 111 MPa, discharge rate of 0.81 m³/min, and power of 1,853 KW.

The cutting depth and cutting volume curves under different displacements and nozzle diameters were compiled and plotted based on over 100 calculation cases. The isobar curves and the applicability range for different models of fracturing trucks were also outlined, as shown in Fig. 30. The results showed displacement and pump pressure increased linearly with the cutting depth and cutting volume when the nozzle diameter remained fixed, which suggests that increasing the pump pressure and displacement of the fracturing truck could enhance cutting efficiency in the actual abrasive jet cutting process. However, since pressure pumps cannot provide unlimited pump pressure, displacement, and power in practical operations, it is necessary to choose corresponding working conditions based on actual circumstances.

The four isobar curves at 40 MPa, 60 MPa, 80 MPa, and 100 MPa showed that under the condition of the same pump pressure, increasing the nozzle diameter inevitably
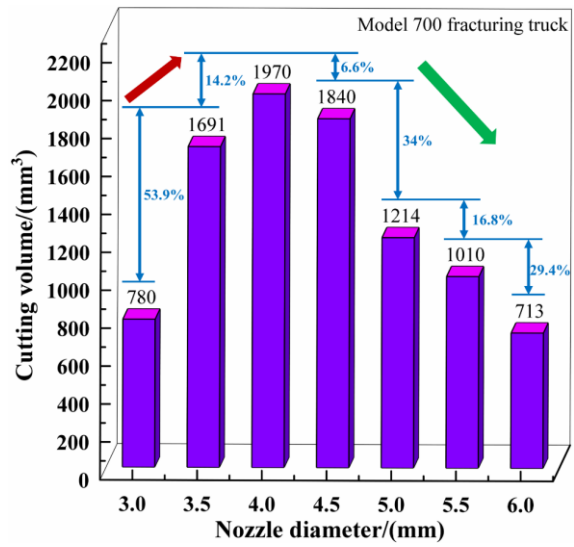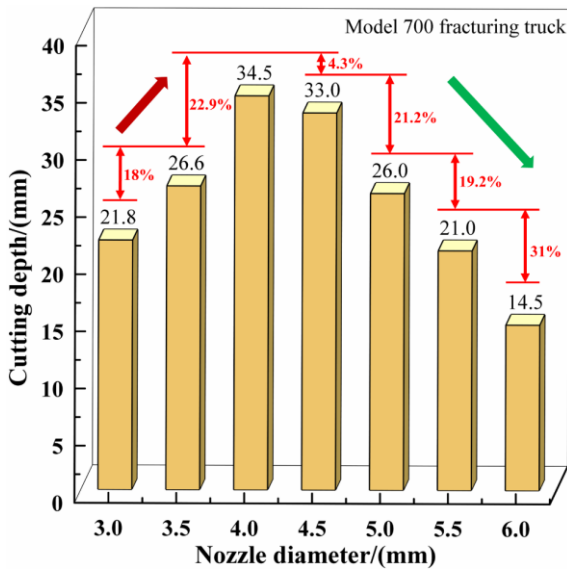
Fig. 26 Cutting depth and cutting volume for different nozzle diameters of the 700 model fracturing vehicle
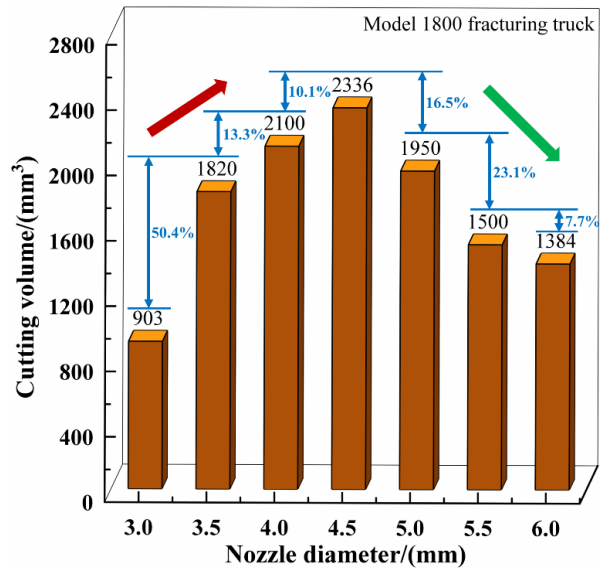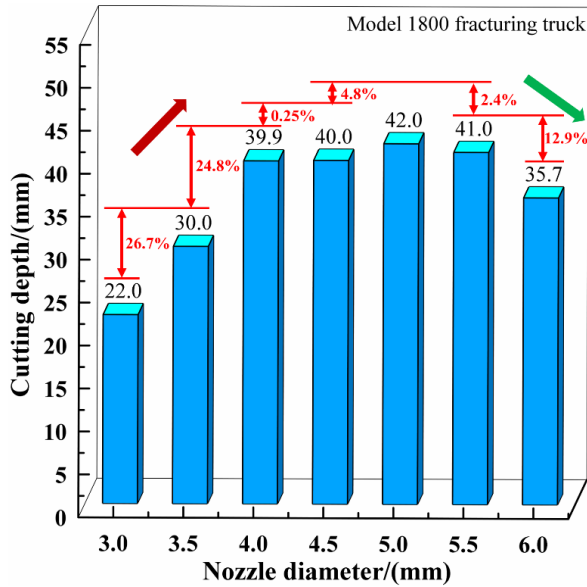
Fig. 27 Cutting depth and cutting volume for different nozzle diameters of the 1800 model fracturing vehicle
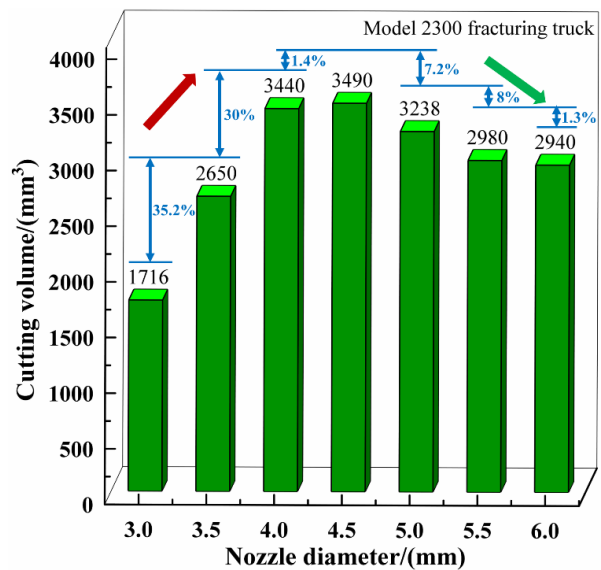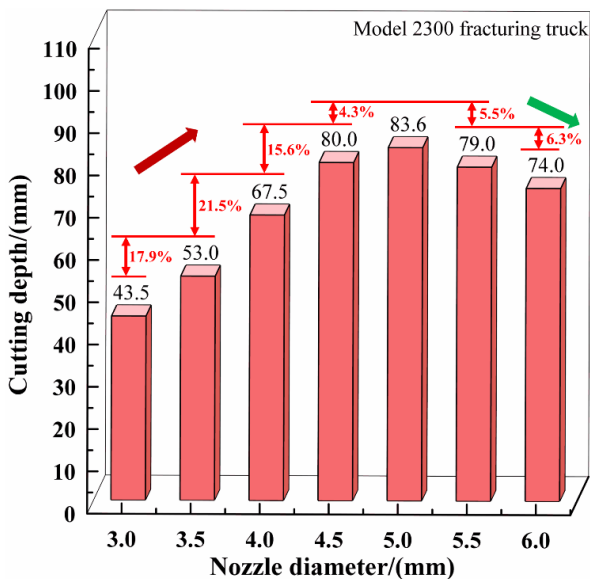
Fig. 28 Cutting depth and cutting volume for different nozzle diameters of the 2300 model fracturing vehicle
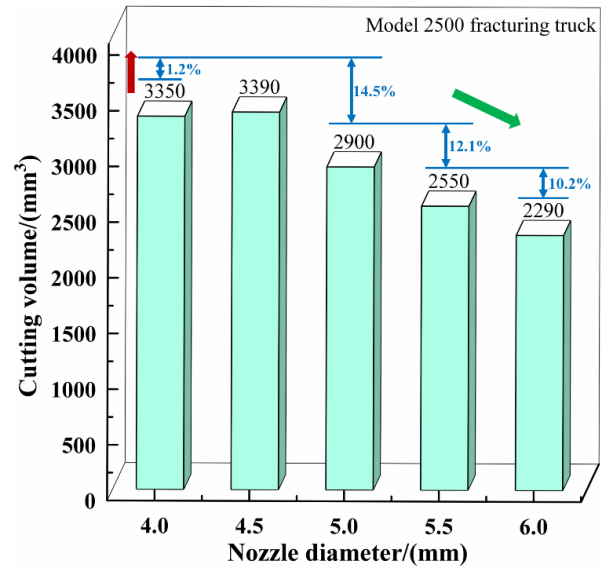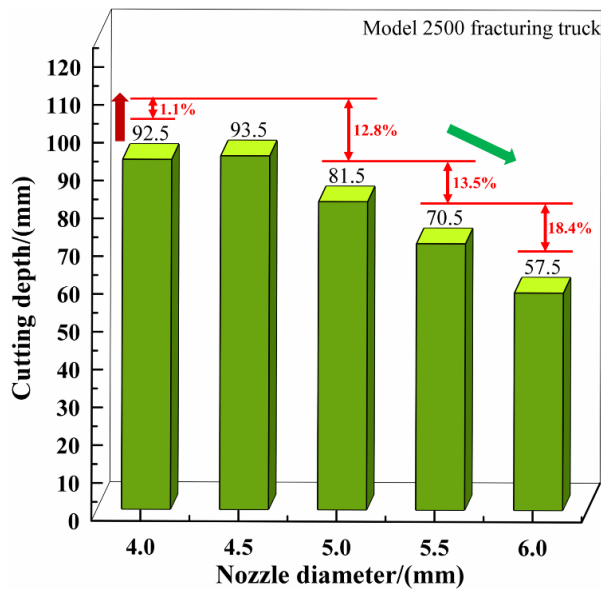
Fig. 29 Cutting depth and cutting volume for different nozzle diameters of the 2500 model fracturing vehicle
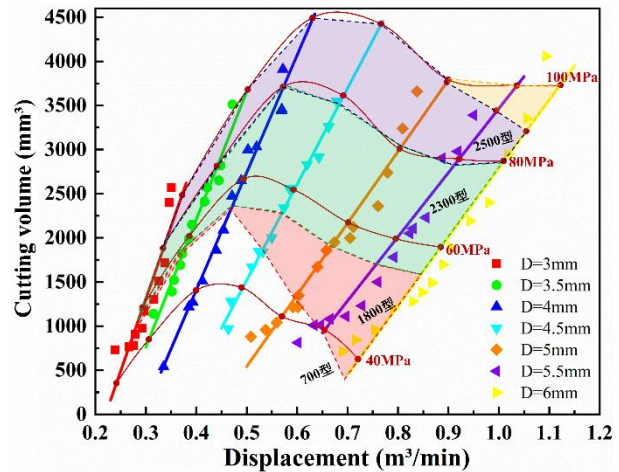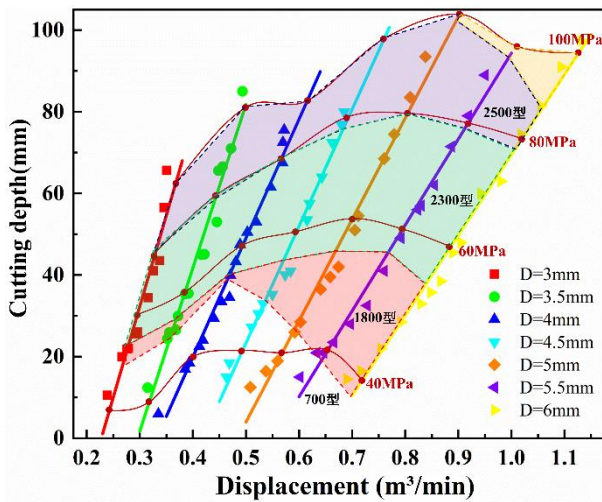
Fig. 30 Cutting depth and cutting volume curves vary with nozzle diameter under varying displacements

resulted in increased displacement, accompanied by the increase in the power output by the pressure pump. However, calculation results indicated that both cutting depth and cutting volume first increased and then decreased. Combined with formulas 11 and 12, which indicate energy loss was proportional to the square of displacement, increasing displacement led to a sharp increase in jet energy loss. Formula 17 shows that jet velocity was inversely proportional to the square of nozzle diameter, indicating that increasing nozzle diameter drastically reduced jet velocity (impact force).

Based on the aforementioned research results, different specifications of fracturing trucks correspond to an optimal nozzle diameter in practical cutting operations. At this optimal nozzle diameter, the highest cutting efficiency can be achieved, thereby maximizing economic benefits. In conclusion, pump pressure, displacement, and nozzle diameter were mutually interactive and influential in the abrasive jet cutting process. Therefore, control variables could not be employed for research purposes. In practical cutting operations, nozzle diameter should be selected based on the pressure pump to achieve optimal cutting efficiency.

4. CONCLUSIONS

1) Utilizing the SPH-FEM method, a novel approach was employed to establish an infinite SPH particle segmentation model, distinguishing itself from the conventional finite SPH particles. This optimized computational method not only reduces the computation time but also verifies the feasibility of AWJ cutting on steel.

2) By analyzing the principles of fluid flow, the interaction relationship between pump pressure, displacement, and nozzle diameter in the process from the pressure pump to the nozzle outlet was studied. Taking into account the resistance losses, precise calculation formulas for these parameters were derived, providing reliable data for subsequent simulation calculations.

3) The cutting efficiency is influenced by the structure of the nozzle, and a tapered nozzle is preferred for cutting operations. The conduit length of the tapered nozzle has little impact on AWJ cutting. A smaller taper angle may lead to clogging, while a larger taper angle

could result in excessive energy loss during the jetting process. The recommended optimal taper angle for a tapered nozzle is approximately 40°.

4) Under different cutting conditions, the optimal range of abrasive concentration varied. Additionally, in the abrasive jet cutting process, with the increase of displacement, the optimal abrasive concentration also increased accordingly.

5) Under a constant pump pressure, increasing the nozzle diameter could lead to a situation where cutting efficiency initially increased and then decreased. Higher cutting efficiency could be achieved in the high-pressure AWJ process with pump pressure ranging from 40 MPa to 100 MPa and nozzle diameter ranging from 4 mm to 5 mm.

CONFLICT OF INTEREST

The authors declare that they have no known competing financial interests or personal relationships that could have appeared to influence the work reported in this paper.

AUTHORS CONTRIBUTIONS

Xiaohua Zhu: Conceptualization, Methodology, Software, Data Curation, Validation, Supervision; **Zhe Luo:** Writing – Original Draft, Methodology, Formal Analysis, Data Curation, Writing – Review & Editing; **Yuan Luo:** Resources, Writing – Review & Editing; **Changshuai Shi:** Formal Analysis, Investigation, Data Curation; **Liuyang Wang:** Resources, Validation.

FUNDING

REFERENCES

Ahmet, H., Çaydaș, U., & Gürün, H. (2006). Effect of traverse speed on abrasive waterjet machining of Ti–6Al–4V alloy. *Materials and Design, 28*,1953-1957. https://doi.org/10.1016/j.matdes.2006.04.020

Akkurt, A. (2010). Cut front geometry characterization in cutting applications of brass with AWJ. *Journal of Materials Engineering and Performance, 19*, 599-606. https://doi.org/10.1007/s11665-009-9513-8

Akkurt, A., Kemal, K. M., & Ulvi, S. (2004). Effect of feed rate on surface roughness in abrasive waterjet cutting applications. Journal of Materials Processing Technology, *147*, 389-396. https://doi.org/10.1016/j.jmatprotec.2004.01.013

Antuono, M., Colagrossi, A., & Bouscasse, B. (2012). Particle packing algorithm for SPH schemes. *Computer Physics Communications, 183*, 1641-1653. https://doi.org/10.1016/j.cpc.2012.02.032

Babu, M. K., & Chetty, O. V. K. (2006). A study on the use of single mesh size abrasives in abrasive waterjet machining. *The International Journal of Advanced Manufacturing Technology, 29*, 532-540. https://doi.org/10.1007/s00170-005-2536-x

Bitter, J. G. A. (1963). A study of erosion phenomena. *Wear, 6*, 5-21. https://doi.org/10.1016/0043-1648(63)90073-5

Boud, F., Loo, L. F., & Kinnell, P. K. (2014). The impact of plain waterjet machining on the surface integrity of Aluminium 7475. *Procedia CIRP*, 13, 382-386. https://doi.org/10.1016/j.procir.2014.04.065

Cai, C., Wang, X. C., & Yuan, X. H. (2019). Experimental investigation on perforation of shale with ultra-high pressureAWJ: Shape, mechanism and sensitivity. *Journal of Natural Gas Science and Engineering, 67*, 196-213. https://doi.org/10.1016/j.jngse.2019.05.002

Chu, W. H., Zhu, D. J., & Liang, D. L. (2018). Dynamic characteristics of three-dimensional complex structure based on coupling algorithm. *Explos Shock Waves, 38*, 725–734. https://doi.org/10.11883/bzycj-2016-0283

Crespo, A. J. C., Domínguez, J. M., & Rogers, B. D. (2015). DualSPHysics: open-source parallel CFD solver based on smoothed particle hydrodynamics (SPH). *Computer Physics Communications, 187*, 204-216. https://doi.org/10.1016/j.cpc.2014.10.004

Demiral, M., Abbassi, F., & Saracyakupoglu, T. (2022). Damage analysis of a CFRP cross-ply laminate subjected toAWJ cutting. *Alexandria Engineering Journal, 61*, 7669–7684. https://doi.org/10.1016/j.aej.2022.01.018

ElTobgy, M. S., Ng, E., & Elbestawi, M. A. (2005). Finite element modeling of erosive wear. *International Journal of Machine Tools and Manufacture, 45*, 1337-1346. https://doi.org/10.1016/j.ijmachtools.2005.01.007

Gunamgari, B. R., & Kharub, M. (2022). Experimental investigation onAWJ cutting of high strength aluminium 7068 alloy. *Materials Today: Proceedings, 69*, 488-493. https://doi.org/10.1016/j.matpr.2022.09.180

Hashish, M. (1984). Cutting with abrasive waterjets. *Mechanical Engineering 106*, 60–69.

Hashish, M. (1989). Pressure effects in abrasive-waterjet (AWJ) machinin. *Journal of Engineering Materials and Technology, 111*, 221-228 . https://doi.10.1115/1.3226458

Hashish, M. (1995). Material properties in abrasive-waterjet machining. *Journal of Engineering for Industry, 117*, 578-583. https://doi.10.1115/1.2803536

Hu, Y. G., Lu, W. B., & Chen, M. (2015). Implementation and verification of SPH-FEM coupling blasting damage analytical method. *Chinese Journal of Rock Mechanics and Engineering, 34*, 2740-2748.

https://doi.org/10.13722/j.cnki.jrme.2014.0104

Jegaraj, J. J. R., & Babu, N. R. (2005). A strategy for efficient and quality cutting of materials with abrasive waterjets considering the variation in orifice and focusing nozzle diameter. *International Journal of Machine Tools and Manufacture, 45*, 1443-1450. https://doi.org/10.1016/j.ijmachtools.2005.01.020

Murugesh, L., & Scattergood, R. O. (1990). Effect of indentation load on fragmentation of erosion particle tips. *Wear, 141*, 115-124. https://doi.org/10.1016/0043-1648(90)90196-H

Natarajan, Y., & Pradeep, K. M. (2017). Study and evaluation ofAWJ cutting performance on AA5083-H32 aluminum alloy by varying the jet impingement angles with different abrasive mesh sizes. *Machining Science and Technology, 21*, 385-415. https://doi.org/10.1080/10910344.2017.1283958

Niranjan, C. A., Srinivas, S., & Ramachandra, M. (2018). Effect of process parameters on depth of penetration and topography of AZ91 magnesium alloy inAWJ cutting. *Journal of Magnesium and Alloys, 6*, 366-374. https://doi.org/10.1016/j.jma.2018.07.001

Pozzetti, G. & Peters, B. (2018). A numerical approach for the evaluation of particle-induced erosion in an abrasive waterjet focusing tube. *Powder Technology, 330*, 229-242. https://doi.org/10.1016/j.powtec.2018.04.006

Soori, M., & Arezoo, B. (2024). Minimization of surface roughness and residual stress in abrasive water jet cutting of titanium alloy Ti6Al4V. *Proceedings of the Institution of Mechanical Engineers, Part E: Journal of Process Mechanical Engineering, 238*(4), 1613-1625. https://doi.org/10.1177/09544089231157972

Thakur, P. M., & Raut, D. N. (2023). Experimental investigation on surface topography in submerged abrasive waterjet cutting of Ti6Al4V. *Advances in Industrial and Manufacturing Engineering, 6*, 100113. https://doi.org/10.1016/j.aime.2023.100113

Tian, J. L., Hu, Z. C., & Liu, S. (2021). Simulation analysis and experimental research of abrasive water jet. *Fluid Machinery, 49*, 1005-0329.

Vikas, B. G., & Srinivas, S. (2020). Kerf analysis and delamination studies on glass-epoxy composites cut byAWJ. *Materials Today: Proceedings,* 2214-7853. https://doi.org/10.1016/j.matpr.2020.09.683

Yang, S., Zhu, X. Y., & Wang, H. (2019). Error characteristic analysis of jet impact momentum law test apparatus based on a SPH-FEM coupling algorithm. *Journal of Vibration and Shock, 38*:253-260. https://doi.org/10.13465/j.cnki.jvs.2019.16.036

Yuvaraj, N., & Kumar, M. P. (2016). Cutting of aluminium alloy with abrasive water jet: and cryogenic assisted abrasive water jet: A comparative study of the surface integrity approach. *Wear, 362-363*, 18-32. https://doi.10.1016/j.wear.2016.05.008

Zhao, H. H., Jiang, H. X., & Warisawa, S. N. C. (2023). Numerical study ofAWJ rotational slits in hard rock using a coupled SPH-FEM method. *Powder Technology, 426*, 118622. https://doi.10.1016/j.powtec.2023.118622

Zhao, N., Xue, P., & Li, Y. L. (2010). Study on dynamic response of honeycomb sandwich panels subjected to bird i mpact. *Acta Armamentarii, A1*, 184-189.